RSC Advances

PAPER

View Article Online
View Journal | View Issue

Check for updates

Cite this: *RSC Adv.*, 2026, **16**, 25503

Microinjection molded PLA/ZnO-TiO_2 composites with *in situ* fibrillation: achieving mechanical matching cortical bone and enhanced osteoinduction

Yong Xiang,† Wenhao Song,† Hui Yang, He Cai, * Yijun Li * and Tao Hu *

Polylactic acid (PLA) has emerged as a cornerstone material in bone tissue engineering due to its biocompatibility and processability. Nevertheless, critical limitations persist, including thermal deformation susceptibility and inadequate osteoinductive capacity, which collectively hinder its clinical translation for load-bearing applications. Herein, we engineer a microinjection molded PLA@ZnO-TiO_2 composite bone fixation plate that simultaneously addresses these challenges through innovative interfacial engineering. The high shear stress during microinjection processing induces *in situ* fibrillation of ZnO-TiO_2 hybrids, generating a unique oriented structure which promoted the interaction of the interfaces between the PLA and ZnO-TiO_2. All samples demonstrated elastic moduli greater than 1.2 GPa, consistent with the specification of human cortical bone. In addition, a uniform spatial distribution of Zn was also observed. The PLA@6%ZnO-TiO_2 composite maintained a uniform Zn^{2+} release concentration ranging from 0.62 to 1.88 μM under vitro conditions, a bioactive range that effectively supported osteoblast proliferation and differentiation. This unique hierarchical architecture and bioactive Zn^{2+} ions synergistically enhanced the *in vitro* cell attachment. The PLA@6%ZnO-TiO_2 composite resulted in a 34.5% increase in ALP activity and 200.1% increase in mineralization levels compared to the control group, indicating its strong potential to promote osteogenic differentiation. Our work establishes a paradigm-shifting manufacturing strategy that transcends conventional composite design, offering dual-phase optimization of structural reliability and biological functionality for future resorbable orthopedic implants.

Received 13th October 2025
Accepted 21st April 2026

DOI: 10.1039/d5ra07812a

rsc.li/rsc-advances

Open Access Article. Published on 18 May 2026. Downloaded on 6/14/2026 9:49:24 PM.
This article is licensed under a Creative Commons Attribution-NonCommercial 3.0 Unported Licence.

1 Introduction

Bone fractures represent a global healthcare challenge. Especially, for short bone fractures like wrist and vertebral, the prevalence of fractures increased by 50% to 100% from 1999 to 2020.[1] Notably, 5–10% of fractures progress to delayed union or nonunion, triggering severe clinical complications, diminished quality of life, and substantial socioeconomic burdens.[2] Currently, internal fixation treatment is the most common and effective surgical treatment for bone fractures.[3] The traditional internal fixation plates are usually made of alloy or ceramic materials, which have good mechanical properties but poor bone induction properties.[4,5] And a second operation is needed to remove the non-absorbable alloy or ceramic materials, increasing the medical burden.[6] Although absorbable polymers address biodegradability concerns, current formulations often sacrifice critical mechanical performance and poor bone induction properties,[7] particularly for micro-fracture fixation requiring millimeter-scale precision. Thus, developing internal fixation plates for short bone fractures that simultaneously achieve appropriate degradation, mechanical integrity, and osteoinductivity remains a significant challenge.

Absorbable polymer materials with excellent biocompatibility and degradability have been the main development direction of modern medical devices.[6] However, traditional processing methods are relatively cost- and time-consuming, especially for micro products with small size and high precision.[8] Microinjection molding technology emerges as a transformative manufacturing paradigm combining rapid production cycles (injection rates up to 1200 mm s^{-1}, cooling times <1 s) with micron-level resolution[9,10] has been widely used in the biomedical field of tissue engineering, biochips, and medical devices, such as micro pumps, blood vessel clips, micro catheters, *etc.*[11,12] This technology's unique shear-induced orientation effects (shear rates >10^7 s^{-1}) enable precise control over polymer crystallinity and fiber alignment, crucial

State Key Laboratory of Oral Diseases & National Clinical Research Center for Oral Diseases & Department of Preventive Dentistry, West China Hospital of Stomatology, State Key Laboratory of Polymer Materials Engineering, Polymer Research Institute, Sichuan University, 610000, China. E-mail: caihe.dr@scu.edu.cn; Ruddph@gmail.com; hutao@scu.edu.cn; Tel: +086-85503486

† The authors contributed equally to this work.

© 2026 The Author(s). Published by the Royal Society of Chemistry

Open Access Article. Published on 18 May 2026. Downloaded on 6/14/2026 9:49:24 PM. This article is licensed under a Creative Commons Attribution-NonCommercial 3.0 Unported Licence.

for enhancing the anisotropic mechanical properties required in bone fixation devices.[13] Microinjection molding is not only a cost- and time-saving method but also ensures high processing accuracy of micro molded products.[13,14]

Polylactic acid (PLA) is widely used in bone tissue engineering for biodegradability and biocompatibility,[15] which is suitable for microinjection molding.[16] However, PLA lacks intrinsic osteoinductive capacity and demonstrates limited efficacy in stimulating osteogenic differentiation.[17] The lower molecular weight hybrid binary metal oxide has been proposed due to its synergistic bio functions, antibacterial properties, and capacity to bind proteins or osteoinductive growth factors.[18] Nano zinc oxide (ZnO) has emerged as a promising absorbable, safe, and nontoxic metal,[6,19] not only performing antibacterial properties,[20] but also capable of promoting bone growth.[21] However, ZnO nanoparticles demonstrate inherent nanoscale aggregation tendencies, resulting in heterogeneous ionic dispersion profiles and nonlinear zinc release kinetics during dissolution processes.[22]

To overcome the critical challenge of nanoparticle agglomeration, we introduced a conceptually novel approach which immobilized ZnO nanoparticles onto fibrous titanium dioxide (TiO_2) substrates *via* a hydrothermal method. The fibrous TiO_2 architecture could provide physical confinement and interfacial charge interactions that effectively suppress ZnO aggregation,[23,24] ensuring more uniform dispersion within the PLA matrix during subsequent microinjection molding. Therefore, the central hypothesis of this work was that this hybrid ZnO-TiO_2 filler system, combined with the unique shear conditions of microinjection molding, would achieve three synergistic outcomes, including uniform filler distribution and controlled Zn^{2+} release kinetics, mechanical properties matching human cortical bone requirements, and significantly improved osteoinductive activity through combined physical (structural support) and chemical (Zn^{2+}) signaling.

Herein, the PLA-based composites incorporating TiO_2 and ZnO-TiO_2 hybrids at varying loadings were systematically investigated. All samples were fabricated *via* microinjection molding to achieve the precise geometries required for short bone fixation plates. The performance of the materials was comprehensively characterized, with particular emphasis on establishing structure–property relationships and elucidating the mechanisms underlying osteogenic differentiation. This work advanced the field by demonstrating that microinjection molding-driven interfacial engineering of hybrid metal oxide fillers could simultaneously resolve the manufacturing constraints and material deficiencies that have limited previous absorbable fixation systems, thereby addressing both the biological compatibility needs and osteoinductive requirements of micro-fracture repair.

2 Materials and methods

2.1 Materials

PLA ($M_w = 30\,000$) was obtained from Dai Gang Biology, China. The zinc acetate dihydrate, triethylamine, and isopropanol were supplied by Shanghai Macklin Biochemical Co.,Ltd. The fibrous TiO_2 was prepared from Shanghai Macklin Biochemical Co.,Ltd.

2.2 Preparation of ZnO-TiO_2 samples

Zinc acetate dihydrate (11 g) was first dissolved in preheated isopropanol (500 mL, 70 °C) under continuous magnetic stirring. Triethylamine (7 mL) was then introduced *via* dropwise addition into the homogeneous mixture. The reaction system was maintained under continuous agitation in a water bath (80 °C) for 10 minutes to ensure complete precursor interaction, followed by a 3 hours static phase at ambient temperature. The resulting solution (50 mL aliquot) was subsequently combined with TiO_2 powder (0.1 g) in a reaction dish to facilitate ZnO-TiO_2 composite formation through heterogeneous nucleation. Final purification involved absolute ethyl alcohol washing and vacuum drying at 120 °C for 1 hour.

2.3 Preparation of PLA, PLA@TiO_2, and PLA@ZnO-TiO_2 samples

PLA composites were prepared by melt-blending with either TiO_2 or ZnO-TiO_2 nanoparticles using a high-speed mixer (Royalstar RS-FS1401, Hefei, China). The weight percentages of TiO_2 or ZnO-TiO_2 nanoparticles in the total mixture were 2%, 4%, and 6%. The compounded materials were then processed through a microinjection molding system (Battenfeld MicroPower-5, Wittmann Battenfeld GmbH, Austria) at injection speeds of 400 mm s^{-1} after plasticization by heating (190 °C). The specimen size for the internal fixation plate was $10 \times 2 \times 0.3$ mm^3 (length × width × thickness). For comparative purposes, pure PLA samples underwent identical processing conditions. Following established nomenclature conventions, the composites were designated as PLA@XTiO_2 or PLA@XZnO-TiO_2, where X indicated the nanoparticle mass percentage relative to the polymer matrix.

2.4 Characterization

Microstructural analysis was conducted using an FEI Inspect F field-emission scanning electron microscope (FE-SEM, FEI Company, USA) operated at 5 kV accelerating voltage. The ZnO-TiO_2 composite samples were gold-coated and subsequently analyzed using SEM to verify the successful deposition of ZnO coating on TiO_2 substrates. For polymer composites (PLA, PLA@TiO_2, PLA@ZnO-TiO_2), we conducted cryogenic fracturing by submerging samples in liquid nitrogen (−196 °C) for 30 minutes, followed by selective etching with 0.125 M NaOH to reveal phase morphology. All specimens received 15 nm gold coatings before imaging to prevent surface charging.

The structural characteristics of samples were analyzed by Fourier-transform infrared spectroscopy (FTIR) using a Nicolet 6700 spectrometer (Thermo Fisher Scientific, USA) in transmission mode. Spectra were acquired at room temperature over the wavenumber range of 2000–400 cm^{-1} with a spectral resolution of 4 cm^{-1}.

X-ray diffraction (XRD) was measured by a DX-1000 X-ray diffractometer (Dandong Fangyuan Instrument Factory, China) from 5° to 75° at a scanning rate of 10°/min. All samples for tests were prepared at appropriate sizes of $10 \times 2 \times 0.3$ mm^3

© 2026 The Author(s). Published by the Royal Society of Chemistry

Open Access Article. Published on 18 May 2026. Downloaded on 6/14/2026 9:49:24 PM. This article is licensed under a Creative Commons Attribution-NonCommercial 3.0 Unported Licence.

(length × width × thickness). The samples were heated from 40 °C to 200 °C under a nitrogen atmosphere with a heating rate of 10 °C min^{-1} to evaluate crystallinity by differential scanning calorimetry (DSC, TACo., Ltd, USA).

X-ray photoelectron spectroscopy (XPS) was performed using an AXIS Supra spectrometer (Kratos) with Al-Kα radiation to evaluate interfacial bonding. Binding energies were calibrated to the C 1s peak at 284.8 eV to ensure measurement accuracy.

To evaluate controlled Zn^{2+} release, samples were immersed in 1 mL of culture medium in 24-well plates and incubated under standard conditions (37 °C, 5% CO_2). The medium was refreshed every 48 hours, and supernatants collected on days 2, 7, 14, and 21 were analyzed for Zn^{2+} concentration using inductively coupled plasma optical emission spectroscopy (ICP–OES, Avio 500, PerkinElmer, USA).

TGA test was performed by a TA-Q50 instrument (TA Instruments, USA) with a heating rate of 10 °C min^{-1} from room temperature to 700 °C in an alumina pan, and under a nitrogen atmosphere with a gas flow rate of 60 mL min^{-1}. The thermal resistance index (T_{HR}) was calculated using the follow Equation to quantify this degradation behavior.[25]

$$T_{HR} = 0.49 \times [T_5 + 0.6 \times (T_{30} - T_5)$$

Where T_5 and T_{30} represented the corresponding decomposition temperatures at 5% and 30% weight loss, respectively.

The samples were stretched at a speed of 50 mm min^{-1} by a universal testing machine (Instron Universal Testing Instruments, USA). Dynamic mechanical analysis was conducted with a strain of 10 μm and a frequency of 1 Hz by TA Q850 equipment (TACo., Ltd,USA) in stretching mode. Rectangular specimens (10 mm in length and 2 mm in width) used for the dynamic mechanical testing were cut from the injection samples.

2.5 Cell culture

Prior to cellular experiments, all specimens underwent ethylene oxide sterilization (37 °C, 2 hours) followed by equilibration in complete culture medium under identical thermal conditions. MC3T3-E1 murine pre-osteoblasts (Shanghai Institute of Biochemistry and Cell Biology, Chinese Academy of Sciences) were maintained in α-MEM growth medium (HyClone, USA) containing 10% FBS (HyClone, USA) and 1% penicillin-streptomycin cocktail (HyClone), with routine subculturing in T-25 flasks (Corning) at 37 °C/5% CO_2. Cell passage was conducted every 48 hours at 80–90% confluency using 0.25% trypsin–EDTA solution (HyClone, USA).

2.6 Cell proliferation

The MC3T3-E1 cells were seeded on the surface of specimens at a density of 1×10^4 cells mL^{-1}. After seeding for 1, 3, and 5 days, the cell counting kit-8 (CCK-8, Dojindo) was used to study the cell proliferation. At each timepoint, specimens underwent two PBS (Gibco, USA) rinses to remove non-adherent cells, followed by the addition of fresh medium containing 10% CCK-8 reagent. After a 2 hours incubation under standard culture conditions (37 °C, 5% CO_2), 100 μL of supernatant from each sample was transferred to a 96-well plate. And a microplate reader was used to measure the absorbance of samples by optical density (OD) at 450 nm.

2.7 Cell morphology and adhesion

The cells were seeded on the surface of specimens for 2 days at a density of 1×10^4 cells per mL to study cell morphology. Following adhesion, samples were gently rinsed twice with PBS and fixed in 2.5% glutaraldehyde (Biosharp, China) at 37 °C for 4 hours. A stepwise ethanol dehydration series (Biosharp, China, 30–100%) was then applied, culminating in overnight vacuum desiccation. Prior to SEM imaging, gold-sputtered specimens were prepared at 5 kV.

The cells were seeded on the surface of specimens at a density of 2×10^4 cells per mL for 4 h to study initial cell adhesion. Post-adhesion, specimens underwent sequential processing: two PBS rinses to remove non-adherent cells, followed by 15 minutes fixation in 4% paraformaldehyde (Biosharp, China) under ambient conditions. Permeabilization with 0.5% Triton X-100 (Beyotime, China, 5 min) preceded additional PBS washes. Dual fluorescent staining was performed using FITC-phalloidin (Solarbio, China, 30 min, Yeasen) for actin visualization and DAPI (Solarbio, China, 30 s, dark) for nuclear counterstaining. Fluorescence imaging of cytoskeletal networks (green) and nuclei (blue) was conducted using a fluorescence microscope (Olympus, Japan).

2.8 Alkaline phosphate (ALP) study

The osteogenic differentiation in MC3T3-E1 cells was studied by the ALP activity. The cell at a density of 2×10^4/well was cultured on scaffolds. After 24 h, the regular medium was replaced with the osteogenic induction medium. After 7 and 14 days, the medium was removed, and the samples were washed with PBS. And the samples per group ($n = 4$) underwent PBS washing followed by histochemical staining using an Alkaline Phosphatase Assay Kit (Beyotime, China). The staining results were observed and recorded using a microscope.

2.9 Alizarin Red-S (ARS) assay

The ARS assay test was also conducted to evaluate late-stage osteogenic mineralization, with MC3T3-E1 cells seeded at 2.5×10^4 cells per well in 24-well plates for 21 days osteogenic culture. Then, the cells were washed with PBS before fixing them with 4% paraformaldehyde for 1 h at room temperature. Later, the cell scaffolds were washed with DI water and incubated with 1 mL ARS solution (Beyotime, China) with pH (4.1–4.3) for 1 h at room temperature. After that, the cell scaffolds were washed 3 times with DI water to remove excess dye from the sample, and digital images were taken for analysis. Further, the quantification of staining, 10% cetylpyridinium chloride, was used to extract the dye absorbed, and the absorbance was measured by spectrophotometry at 570 nm.

Open Access Article. Published on 18 May 2026. Downloaded on 6/14/2026 9:49:24 PM. This article is licensed under a Creative Commons Attribution-NonCommercial 3.0 Unported Licence.

2.10 Statistical analysis

All the *in vitro* experiments were triplicated independently, and the statistical analysis of the data was calculated using one-way analysis of variance and Tukey's post hoc analysis program. The data were expressed as the mean ± standard deviation, and the p values marked as $^{*}P < 0.05$, $^{**}P < 0.01$, $^{***}P < 0.001$, $^{****}P < 0.0001$, were considered to be statistically significant.

3 Results and discussion

3.1 Synthesis of PLA@TiO_2/ZnO-TiO_2 microinjection-molded bone fixing plates

As shown in Fig. 1, the SEM analysis confirmed successful deposition of nano ZnO on fibrous TiO_2 without aggregation. Nano ZnO is a promising absorbable, safe, and nontoxic material.[19,26] However, ZnO nanoparticles tend to aggregate at the nanoscale, leading to uneven ion distribution and nonlinear zinc release kinetics during dissolution.[27] To address this limitation, we utilized hydrothermal deposition to grow ZnO crystals directly on fibrous TiO_2 substrates, which could effectively prevented nanoparticle aggregation.[24] A more effective promotion of bone formation with minimized cytotoxicity might be achieved by leveraging the complementary roles of ZnO and TiO_2, where ZnO provided initial osteoinductive stimulation while TiO_2 ensured long-term stability, promoted osseointegration, and regulated ZnO degradation. Critically, polymer composite performance depends not only on biological functionality but fundamentally on the morphology and domain size of constituent phases. For medical applications requiring both mechanical robustness and structural stability, microinjection molding provides an ideal processing solution.[28,29] In our approach, PLA polymer was compounded with either pristine TiO_2 or ZnO-TiO_2 composite powder. This mixture was fed into a microinjection molding system where it underwent: plasticization (melting and homogenization), forward conveyance through the barrel, and high-pressure injection into the mold cavity (Fig. 1b). During injection, significant shear forces develop as the melt flows through the narrow gate and along mold walls. Unlike the traditional low-shear processing methods for PLA-metal oxide composites, this high-shear field induced preferential orientation in both the polymer chains and filler, with this oriented structure being rapidly frozen in place through cooling.[29,30] This structural design also effectively addressed the issue of nanoparticle agglomeration commonly observed in PLA-metal oxide composites.[31,32]

3.2 Microstructural morphology and crystallographic characterization of PLA@TiO_2/ZnO-TiO_2 microinjection-molded bone fixing plates

Processing-induced shear forces *via* microinjection molding promoted both uniform dispersion of TiO_2-based fillers and their directional alignment along the polymer flow front. As confirmed by combined SEM and SAXS characterization (Fig. 2a), this shear-mediated orientation generated hierarchically ordered architectures, through the situ fibrillation of TiO_2-based hybrids. Cross-sectional microscopy (Fig. 2b) revealed parallel arrays of rod-shaped fillers aligned with the flow direction, while EDS elemental maps (Fig. 2c) quantitatively verified homogeneous Ti and Zn distribution throughout the PLA matrix, confirming effective interfacial integration.

Characteristic peaks of metal oxides were further investigated through complementary FTIR and XRD techniques. The FTIR spectra (Fig. 2d) displayed distinct vibrational signatures corresponding to Zn–O and Ti–O bonds between 400–800 cm^{-1}, partially overlapping with PLA's amorphous C–O–C bands at lower wavenumbers. XRD analysis (Fig. 2e) confirmed crystalline TiO_2 through characteristic peaks at 28.7° (110) and 42.4° (111), whose intensities increased proportionally with filler loading. Intriguingly, the observed attenuation of TiO_2 peak

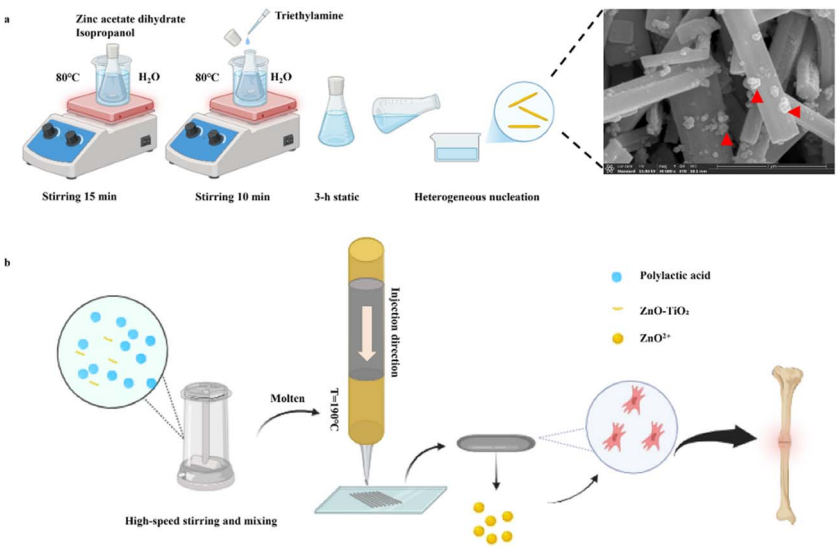

Fig. 1 Synthesis of PLA@TiO_2/ZnO-TiO_2 microinjection molded bone fixing plates. (a) Synthesis of ZnO-TiO_2 samples (red arrow indicates the ZnO crystal). (b) Synthesis of PLA@TiO_2/ZnO-TiO_2 bone fixing plates.

© 2026 The Author(s). Published by the Royal Society of Chemistry

Open Access Article. Published on 18 May 2026. Downloaded on 6/14/2026 9:49:24 PM.
This article is licensed under a Creative Commons Attribution-NonCommercial 3.0 Unported Licence.

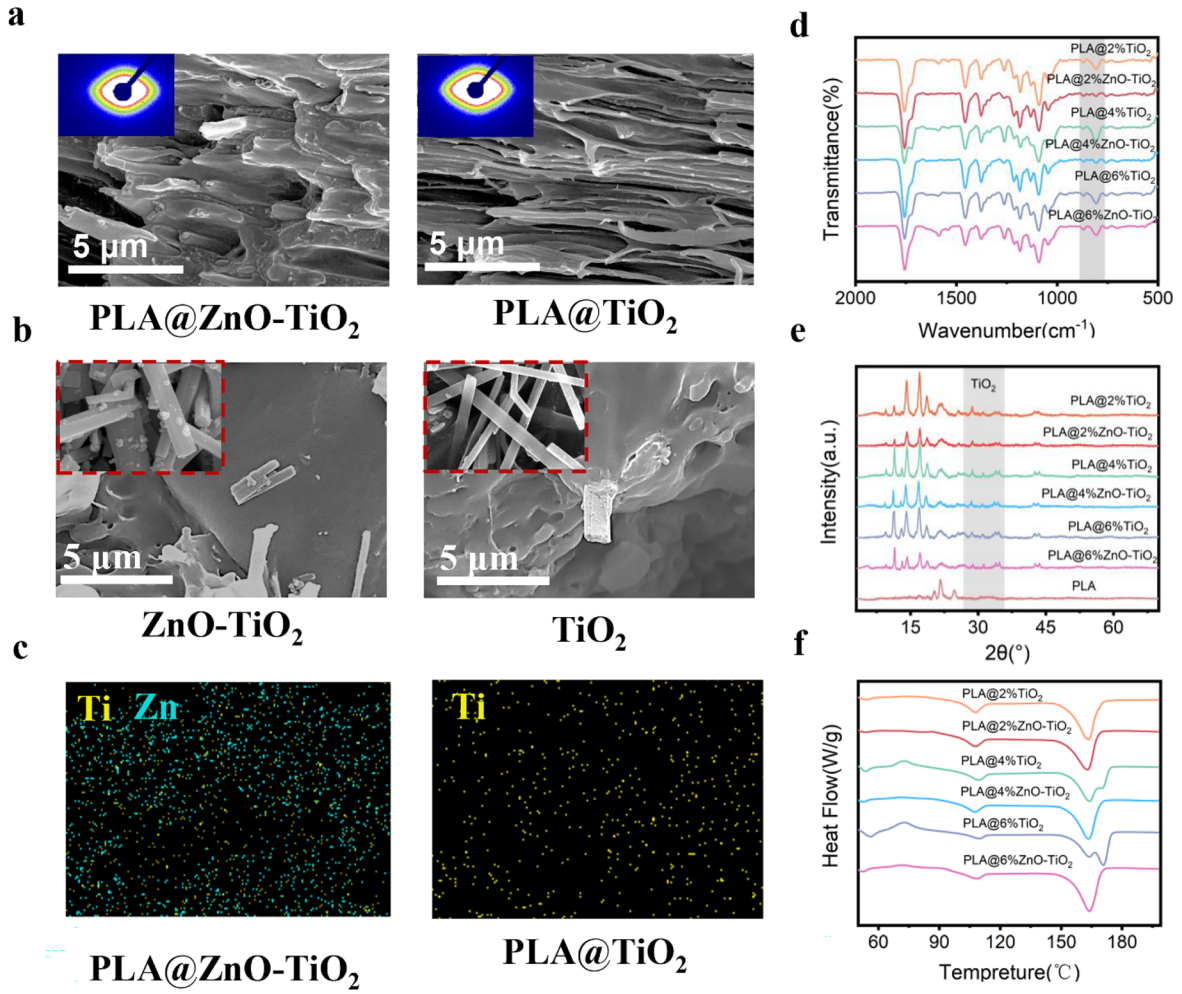

Fig. 2 Microstructural morphology and crystallographic characterization of PLA@TiO_2/ZnO-TiO_2 bone fixing plates. (a) Cross-sectional SEM morphology and SAXS profile (inset) of microinjection molded bone fixing plates with 6 wt% filler concentration. (b) Comparative SEM micrographs of pristine TiO_2 and ZnO-TiO_2 fillers (insets) and their post-processed counterparts. (c) EDS elemental mapping illustrating homogeneous Ti and Zn spatial distribution. (d) FTIR spectra and (e) XRD patterns of osteogenic devices across varying filler concentrations. (f) DSC thermograms of bone fixing plates with incremental filler loadings.

intensities at equivalent concentrations revealed ZnO's shielding effect. X-ray absorption by surface ZnO layers reduced penetration depth to underlying TiO_2 substrates, providing direct evidence of ZnO deposition. Morphological evaluation (Fig. 2b) verified the preservation of fibrous TiO_2 cores with conformal ZnO coatings, maintaining structural integrity during high-shear processing. DSC thermograms (Fig. 2f) further corroborated crystallinity retention, showing distinct melting endothermic peaks in all samples during heating. This further identified that shear-induced polymer chain alignment during microinjection molding created an ordered architecture.

Nano-ZnO particles exhibit a strong tendency to agglomerate when employed in isolation, with elevated concentrations potentially inducing cytocompatibility concerns.[33] This inherent aggregation characteristic significantly compromises their effectiveness when utilized for polymer nanofiber film modification. The study coated ZnO on fibrous TiO_2, which could avoid agglomeration.[34] Compared to the direct incorporation of ZnO nanoparticles into PLA, this design resulted in a more uniform and sustained release of Zn^{2+}, thereby avoiding the cytotoxic effects associated with burst release.[35] Under mechanical processing conditions involving stretching or shear forces, these well-dispersed linear ZnO-TiO_2 composites spontaneously organize into oriented microfibrillar structures. This alignment mechanism transforms the composite system into a rigid reinforcing phase with anisotropic mechanical enhancement capabilities.[36] The shear-induced oriented fibrillar structure of ZnO-TiO_2 could serve as a mechanically compatible scaffold for bone regeneration, while simultaneously providing a topographical cue to guide cell behaviour.

These results verify the effective integration and ordered distribution of TiO_2-based fillers within the PLA matrix. This hierarchically ordered architecture proves critical for physiological stability, as crystalline domains resist enzymatic erosion longer than amorphous regions in simulated body fluid. And the hierarchical ordered architecture creates a bioactive scaffold that not only provides structural support but also actively recruits bone cells, accelerating new tissue growth while

Open Access Article. Published on 18 May 2026. Downloaded on 6/14/2026 9:49:24 PM.
This article is licensed under a Creative Commons Attribution-NonCommercial 3.0 Unported Licence.

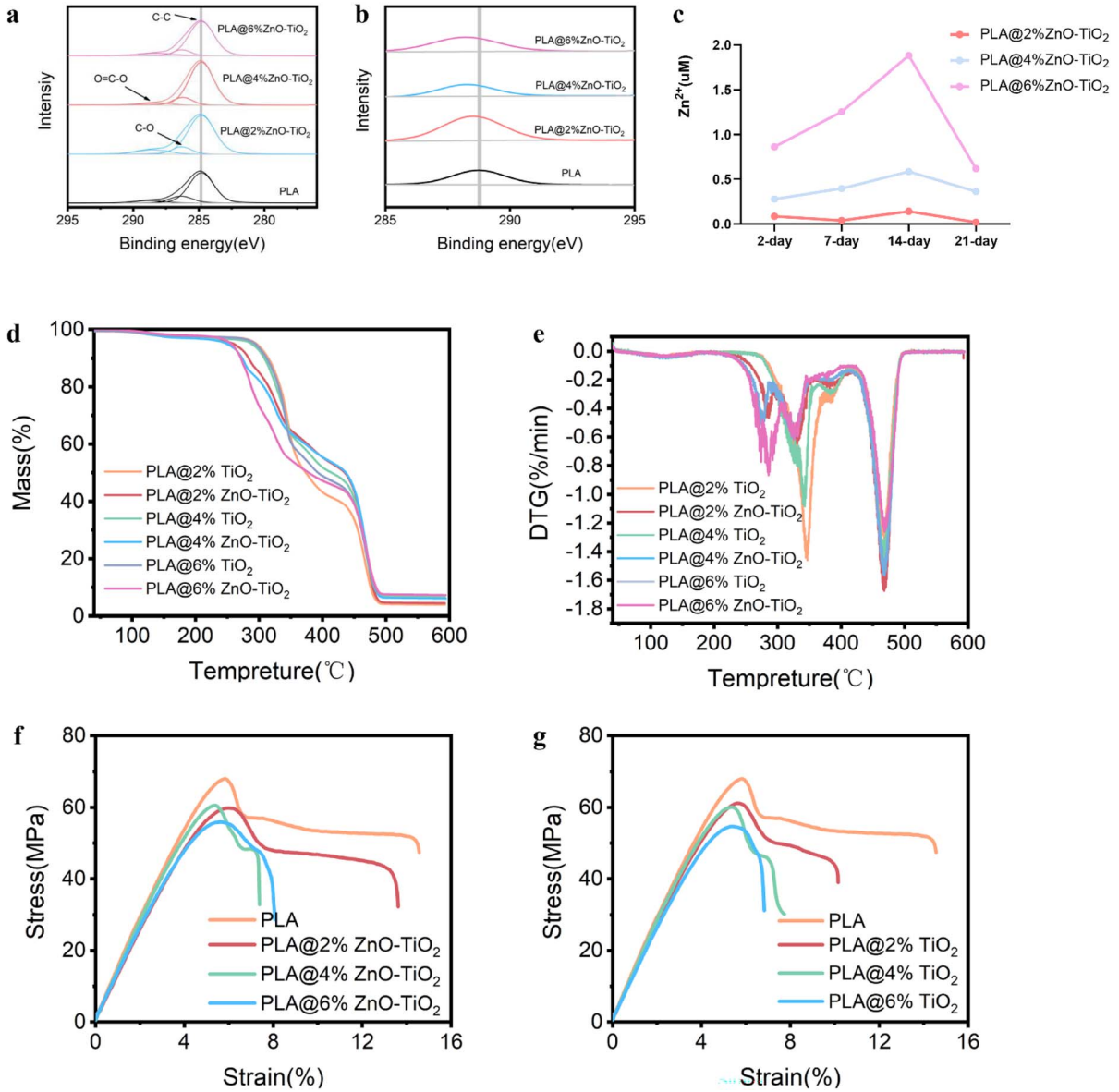

Fig. 3 Interfacial interactions, Zn^{2+} released, thermal stability and mechanical properties of PLA@TiO_2/ZnO-TiO_2 bone fixing plates. (a) and (b) XPS spectra, (c) Zn^{2+} released, (d) thermogravimetric and (e) derivative thermogravimetric curves, alongside (f) and (g) stress–strain profiles.

preventing infection. As the PLA gradually breaks down, the engineered ZnO nanostructures release zinc ions, simultaneously strengthening the composite to maintain mechanical integrity during healing. This multiscale design leverages ZnO's natural bone-healing properties and PLA's biocompatibility within a single optimized system, essentially giving surgeons an 'all-in-one' material that rebuilds bone while minimizing rejection risks.

3.3 Interfacial interactions, Zn^{2+} released, thermal stability and mechanical properties of PLA@TiO_2/ZnO-TiO_2 microinjection-molded bone fixing plates

High-resolution XPS spectra provides key insights into the interfacial interactions within the composites. To minimize the charging effect, the binding energies of all samples were calibrated using the C–C/C–H peak (284.8 eV) as an internal reference, which ensured data comparability (as indicated by the gray dashed line in Fig. 3a). As seen in the high-resolution C 1s spectra (Fig. 3a), the O=C–O peak in the composites showed a small but reproducible shift toward lower binding energy by approximately 0.4–0.7 eV, compared to pure PLA. To better illustrate this trend, a magnified view of the O=C–O peak region was provided (Fig. 3b), clearly showing that the peak shift gradually became more pronounced as the ZnO-TiO_2 filler content increased from 2% to 6%. This systematic change in binding energy pointed to electronic interactions between the carbonyl groups of PLA and the metal oxide surfaces, indicative of coordination-type bonding rather than simple physical mixing.

The concentration of Zn^{2+} released from all samples remained within the bioactive and non-cytotoxic range (0–10 μM)

© 2026 The Author(s). Published by the Royal Society of Chemistry

Open Access Article. Published on 18 May 2026. Downloaded on 6/14/2026 9:49:24 PM. This article is licensed under a Creative Commons Attribution-NonCommercial 3.0 Unported Licence.

Table 1 Thermal characteristics of PLA@TiO_2/ZnO-TiO_2 bone fixing plates[a]

Sample name	T_5/°C	T_{30}/°C	T_{HR}/°C
PLA@2%wt TiO_2	299.84	344.37	160.01
PLA@2%wt ZnO-TiO_2	265.8	336.78	151.11
PLA@4%wt TiO_2	293.18	341.94	157.99
PLA@4%wt ZnO-TiO_2	253.08	331.01	146.92
PLA@6%wt TiO_2	297.27	341.26	158.60
PLA@6%wt ZnO-TiO_2	256.38	309.08	141.12

[a] T_5 and T_{30}, the corresponding decomposition temperatures at 5% and 30% weight loss, respectively; T_{HR}, thermal resistance index.

established for osteoblasts (Fig. 3b).[37,38] Among all groups, the PLA@6%ZnO-TiO_2 composite exhibited the highest Zn^{2+} concentration, while still staying well within the non-cytotoxic threshold. Furthermore, the release increased over the early degradation period (2–14 days), which could be attributed to the greater exposure of ZnO nanoparticles as the PLA matrix progressively degraded. Notably, the composite achieved a more uniform and sustained Zn^{2+} release compared to the direct blending of ZnO nanoparticles in PLA, effectively avoiding the cytotoxicity typically associated with burst release.[39] This was attributed to the fibrous structure and high shear-induced orientation that prevented ZnO agglomeration, as well as interfacial bonding among PLA and the metal oxide surfaces that stabilized ion release.

Orthopedic fixation systems require sustained thermal stability and mechanical integrity throughout bone regeneration phases. Intriguingly, TGA revealed a progressive leftward shift in degradation curves with elevated filler loading (Fig. 3c–d), demonstrating a concentration-dependent thermal degradation profile, as detailed in Table 1. This phenomenon correlates with reduced interfacial molecular interactions between fillers and polymer chains. Notably, PLA@ZnO-TiO_2 composites displayed lower T_{HR} than PLA/TiO_2 counterparts at equivalent filler loadings. This divergence likely stems from ZnO's characteristic surface asperities on fibrous fillers, which perturb polymer-filler interfacial adhesion through localized stress concentrations. Crucially, all T_{HR} values surpassed physiological temperature thresholds, thereby maintaining sterilization-compatible thermal stability while ensuring safe *in vivo* performance. Upon heating to 600 °C, the PLA matrix fully decomposed, leaving only the inorganic fillers as residue. The TGA results confirmed that the residual masses at 600 °C closely corresponded to the nominal loadings of 2%, 4%, and 6% (Table 2). This confirmed the uniform distribution of TiO_2-based fillers within the PLA matrix under high shear field.

Table 2 Residual weight of PLA@TiO_2/ZnO-TiO_2 bone fixing plates by TGA

Sample name	Filler content (wt%)	Residue (wt%)
PLA@2%TiO	2	2.192
PLA@2%ZnO-TiO_2	2	2.282
PLA@4%TiO	4	4.228
PLA@4%ZnO-TiO_2	4	4.132
PLA@6%TiO	6	6.071
PLA@6%ZnO-TiO_2	6	6.238

Notably, the stress–strain profiles (Fig. 3e and f) demonstrated preserved mechanical toughness across increasing TiO_2-based filler loadings, a counterintuitive trend attributable to the shear-induced alignment of fillers creating stress-transfer pathways. All formulations exhibited elastic moduli exceeding 1.2 GPa, matching human cortical bone specifications.[40] These results confirmed the reliability of PLA/TiO_2 and PLA/ZnO-TiO_2 biomaterials in promoting osteoblast growth. This mechanical synergy between oriented reinforcement and bone-mimetic stiffness validated the structural suitability of PLA@TiO_2 composites for osteogenic applications.

3.4 PLA@ZnO-TiO_2 plates support pre-osteoblast cell growth

Following comprehensive characterization of thermal and mechanical properties, we evaluated the cytocompatibility and cellular responses of PLA composites using MC3T3-E1 pre-osteoblasts. CCK-8 viability assays confirmed non-toxicity across all groups, with initial 24 hours adaptation-phase reductions resolving completely by Day 5, demonstrating excellent biocompatibility (Fig. 4a). After culturing for 48 h, the SEM revealed cytoplasmic density granular increases in cells cultured on composites (Fig. 4b). This result suggested an enhanced natural enrichment of organelles or inclusions.[41] A well stretched morphology with filopodia was observed on cells of PLA@ZnO-TiO_2 plates, while cells on the PLA and PLA@TiO_2 groups showed less filopodia (Fig. 4c). The *in situ* fibrillated orientation structure of ZnO-TiO_2 within the PLA matrix presented a topographical bioactive surface, thereby stimulating filopodia extension and cytoskeleton rearrangement in MC3T3-E1 cells. The continuous and safe release of Zn^{2+} also contributed to enhanced cell adhesion and proliferation.[38] Further, based on the results of the initial adhesion assessment, the plates demonstrated better cell number, cell distribution and morphology after seeding, indicating the composite plates supported pre-osteoblast growth, especially for PLA@6%ZnO-TiO_2 group (Fig. 4c).

3.5 PLA@ZnO-TiO_2 plates support pre-osteoblast cell osteogenic differentiation

ALP staining is a trusted method for evaluating ALP expression, an important early marker of osteogenic differentiation. ALP staining showed that PLA@ZnO-TiO_2 groups had higher blue-purple precipitation and relative ALP activity, compared to control, PLA, and PLA@TiO_2 groups (Fig. 5a–d). The PLA@6% ZnO-TiO_2 composite demonstrated a 34.5% increase in ALP activity compared to the control group following 14 days of osteogenic induction, indicating enhanced osteogenic differentiation potential through zinc ion-mediated stimulation (Fig. 5d). After 14 days of osteogenic induction, the ALP activity of PLA@ZnO-TiO_2 composites increased with ZnO loading, correlating with the rising release concentration of Zn^{2+}. This biological response correlates with zinc's dual role as both an enzymatic cofactor in ALP functionality and a critical regulator

Open Access Article. Published on 18 May 2026. Downloaded on 6/14/2026 9:49:24 PM.
This article is licensed under a Creative Commons Attribution-NonCommercial 3.0 Unported Licence.

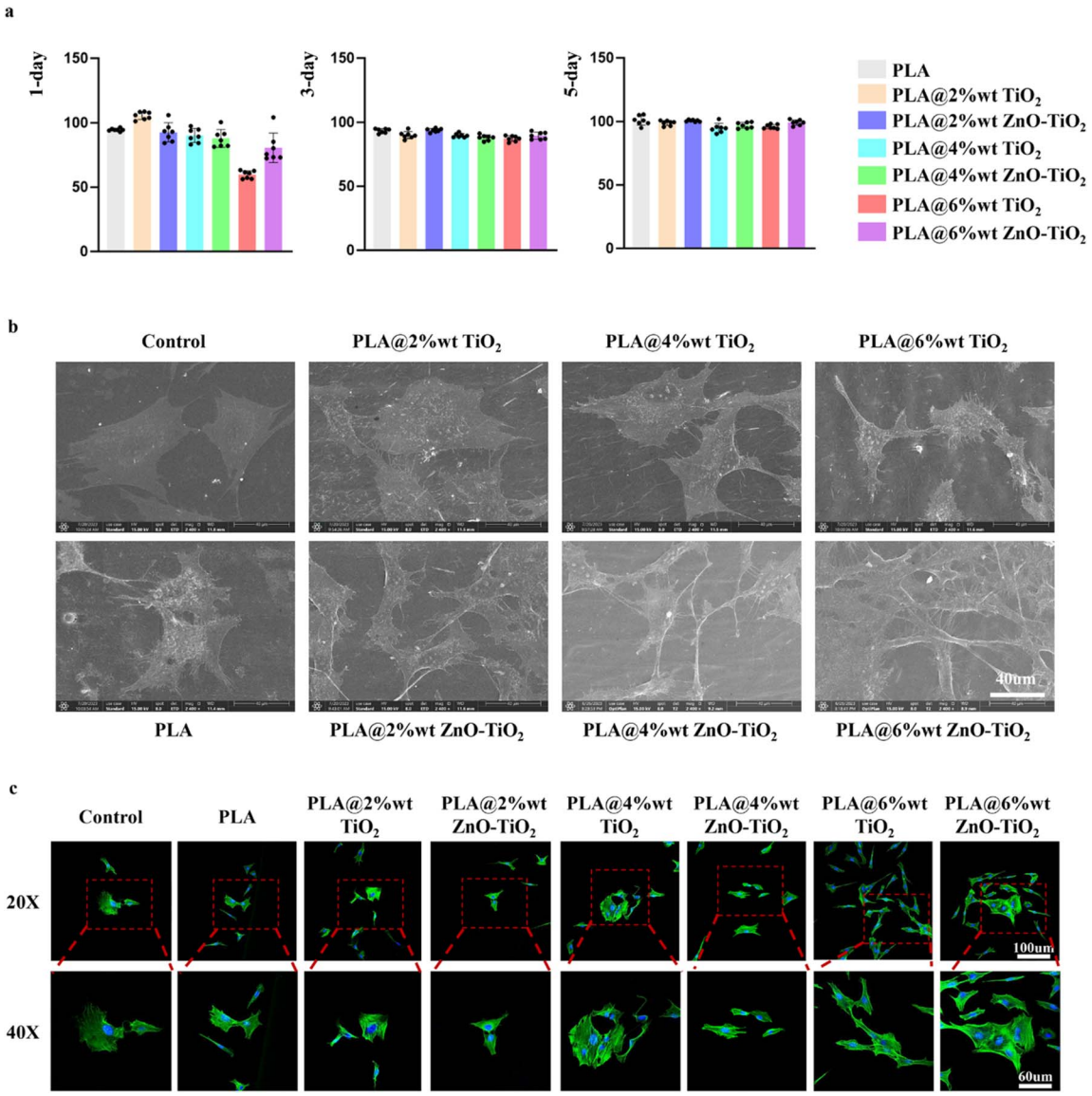

Fig. 4 *In vitro* biocompatibility of PLA@TiO_2/ZnO-TiO_2 bone fixation plates. (a) CCK-8 assay of MC3T3-E1 cells seeded on PLA@TiO_2/ZnO-TiO_2 plates after 1, 3 and 5 days ($n = 7$). (b) Representative SEM images of cells seeded on PLA@TiO_2/ZnO-TiO_2 plates after 2 days. (c) Representative fluorescence images of cells seeded on PLA@TiO_2/ZnO-TiO_2 plates after 4 h. Nuclei, DAPI (blue); F-actin, FITC labeled phalloidin (green). Data are presented as mean ± s.d. Scale bars are 50 μm for panel b; scale bars are 100 μm and 60 μm for 20× and 40× in panel c.

of hydroxyapatite crystallization during bone matrix mineralization.[42]

ARS staining is a trusted method for evaluating calcium salt deposition. The number, size, and distribution of mineralized nodules can reflect the osteogenic activity of osteoblasts and the process of osteogenic differentiation. ARS staining results corroborated the observation that osteogenic cells cultured on PLA@6%ZnO-TiO_2 composite substrates exhibited the extensive distribution of mineralized nodules (Fig. 5e). This observation was further supported by quantitative analysis, which revealed a 200.1% increase in mineralization levels compared to the control group after 21 days of osteogenic induction, demonstrating the composite's superior osteogenic differentiation potential (Fig. 5f). Following 21 days of osteogenic induction, the mineralization levels of the PLA@ZnO-TiO_2 composites showed a ZnO loading-dependent increase, which correlated with the elevated concentrations of released Zn^{2+}. These results demonstrated that strategic integration of ZnO-TiO_2 nanocomponents established an osteoinductive microenvironment, promoting biomineralization through cell-directed extracellular matrix remodeling and calcium phosphate nucleation.

The composite's hierarchical structure, consisting of a PLA matrix and oriented ZnO-TiO_2 fibrils, mimicked the extracellular matrix of bone tissue.[43] This biomimetic architecture actively facilitated osteoblast recruitment and accelerated osteogenic differentiation, representing a significant advancement over the passive support offered by traditional bone

© 2026 The Author(s). Published by the Royal Society of Chemistry

Open Access Article. Published on 18 May 2026. Downloaded on 6/14/2026 9:49:24 PM.
This article is licensed under a Creative Commons Attribution-NonCommercial 3.0 Unported Licence.

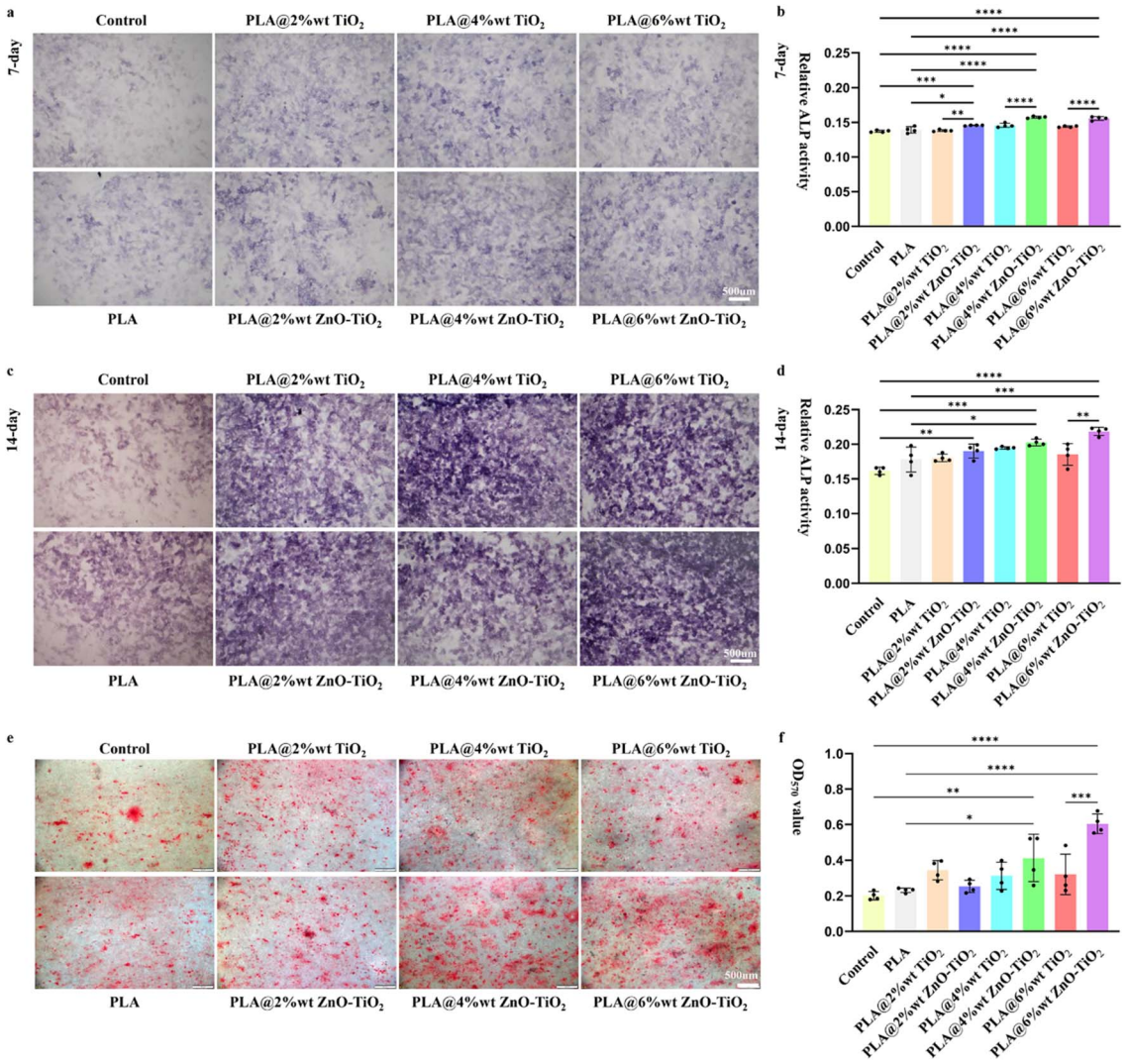

Fig. 5 *In vitro* induction of osteogenic differentiation of PLA@TiO_2/ZnO-TiO_2 bone fixation plates. (a) Representative alkaline phosphatase (ALP) staining images of cells seeded on PLA@TiO_2/ZnO-TiO_2 plates after osteogenic induction 7 days. (b) Statistical analysis results of relative ALP activity after osteogenic induction 7 days ($n = 4$). (c) Representative ALP staining images of cells seeded on PLA@TiO_2/ZnO-TiO_2 plates after osteogenic induction 14 days. (d) Statistical analysis results of relative ALP activity after osteogenic induction 14 days ($n = 4$). (e) Representative alizarin red-S (ARS) staining images of cells seeded on PLA@TiO_2/ZnO-TiO_2 plates after osteogenic induction 21 days. (f) Statistical analysis results of calcium ion concentration (OD_{570}) after osteogenic induction 21 days ($n = 4$). Data are presented as mean ± s.d., *P*-values derived from one-way analysis of variance tests with Tukey's multiple comparisons tests. *: $P < 0.05$; **: $P < 0.01$; ***: $P < 0.001$; ****: $P < 0.0001$. Scale bars are 500 μm for panel a, c, and e.

plates. In addition, the sustained release of Zn^{2+} from the composite functioned as a dual regulator of osteogenic differentiation, enhancing ALP activity as an enzymatic cofactor while simultaneously promoting extracellular matrix mineralization.[42] As a result, the composite plate demonstrated a synergistic enhancement of cell adhesion, osteogenic differentiation, and mineralization *in vitro*. This synergistic effect arose from the combination of its structural support and the bioactive regulation of Zn^{2+} release, in contrast to conventional PLA-metal composites.

Clinically, these findings support PLA@ZnO-TiO_2 as a promising candidate for load-bearing bone fixing plates. The material's hierarchical architecture and dual functionality, specifically structural support from PLA's mechanical integrity coupled with bioactive function, addresses current limitations in bone fixation plates that either passively resorb or lack osteoinductive capacity. Future studies should validate these results in an ovine critical-sized defect model.

4 Conclusions

The PLA-based composites incorporating ZnO-TiO_2 fillers *via* microinjection molding for application as absorbable internal fixation plates in short bone fracture repair were successfully developed. The aggregation of ZnO was effectively prevented by deposition onto fibrous TiO_2 substrates, ensuring remarkably uniform filler distribution within the PLA matrix after micro-injection molding. All samples demonstrated elastic moduli

Open Access Article. Published on 18 May 2026. Downloaded on 6/14/2026 9:49:24 PM. This article is licensed under a Creative Commons Attribution-NonCommercial 3.0 Unported Licence.

exceeding 1.2 GPa, aligning with the specification of human cortical bone. The fibrous ZnO-TiO_2 formed *in situ* by the microinjection process presented significant oriented structure and orderly filler distribution with the PLA matrix. And the concentrations of Zn^{2+} released from all samples were kept within the bioactive and non-cytotoxic range for osteoblasts. This unique hierarchical architecture and bioactive Zn^{2+} ions created a synergistic effect that actively promoted both enhanced cell attachment and accelerated osteogenic differentiation *in vitro* studies. This work established that microinjection molding-driven interfacial engineering of PLA and ZnO-TiO_2 fillers enabled a unique combination of structural support and biological functionality. Beyond the specific materials investigated, this study provided a broadly applicable framework for designing high performance polymer nanocomposites where controlled filler dispersion and synergistic bioactivity are critically required.

Author contributions

Y. X., contributed to writing – original draft and review and editing, visualization, methodology, investigation, formal analysis; W. S., contributed to writing – original draft and review and editing, visualization, methodology, investigation, formal analysis; H. Y., contributed to writing – review and editing, visualization, funding acquisition; H. C., contributed to writing – review and editing, supervision, project administration, funding acquisition, conceptualization; Y. L., contributed to writing – review and editing, supervision, project administration, funding acquisition, conceptualization; T. H., contributed to writing – review and editing, supervision, conceptualization. All authors read and approved the final version of the manuscript.

Conflicts of interest

There are no conflicts to declare.

Data availability

All data supporting the findings of this study are available within the article. Raw data are available from the corresponding author upon reasonable request.

Acknowledgements

The authors would like to thank the Natural Science Foundation of Sichuan Province (No. 2023NSFSC2000), Sichuan Science and Technology Program (No. 2024YFHZ0043), Sichuan University U35 Excellent Young Faculty Team Development and Support Program (No. 1082204112MM27), and Research and Develop Program, West China Hospital of Stomatology Sichuan University (No. RD-03-202401) for supporting this work, and thank Fanzi Wu and Xin Guan (Frontier Innovation Center for Dental Medicine Plus, West China Hospital of Stomatology, Sichuan Uniersity) for fluorescence microscope data acquisition.

Notes and references

1 B. Xu, M. R. Radojčić, D. B. Anderson, B. Shi, L. Yao, Y. Chen, S. Feng, J. H. Lee and L. Chen, Trends in prevalence of fractures among adults in the United States, 1999-2020: a population-based study, *Int. J. Surg.*, 2024, **110**(2), 721–732.
2 K. Zha, M. Tan, Y. Hu, W. Hu, S. Zhang, Y. Zhao, Z. Lin, W. Zhang, H. Xue, B. Mi, *et al*, Regulation of metabolic microenvironment with a nanocomposite hydrogel for improved bone fracture healing, *Bioact. Mater.*, 2024, **37**, 424–438.
3 B. Liu, S. Zhang, Y. Yang, M. Wang, X. Zhang, J. Zhang, W. Qi and L. Yang, An Automatic Personalized Internal Fixation Plate Modeling Framework for Minimally Invasive Curved Bone Fracture Surgery Based on Preregistration With Capsule Projection Model, *IEEE Trans. Biomed. Eng.*, 2020, **67**(3), 706–717.
4 M. Niinomi, Y. Liu, M. Nakai, H. Liu and H. Li, Biomedical titanium alloys with Young's moduli close to that of cortical bone, *Regen. Biomater.*, 2016, **3**(3), 173–185.
5 C. Zhang, P. Wen, Y. Xu, Z. Fu and G. Ren, Exploring Advanced Functionalities of Carbon Fiber-Graded PEEK Composites as Bone Fixation Plates Using Finite Element Analysis, *Materials*, 2024, **17**(2), 414.
6 B. Huang, M. Yang, Y. Kou and B. Jiang, Absorbable implants in sport medicine and arthroscopic surgery: A narrative review of recent development, *Bioact. Mater.*, 2024, **31**, 272–283.
7 C. Garot, G. Bettega and C. Picart, Additive Manufacturing of Material Scaffolds for Bone Regeneration: Toward Application in the Clinics, *Adv. Funct. Mater.*, 2021, **31**(5), 2006967.
8 R. Mau, T. Eickner, G. Jüttner, Z. Gao, C. Wei, N. Fiedler, V. Senz, T. Lenarz, N. Grabow, V. Scheper, *et al*, Micro Injection Molding of Drug-Loaded Round Window Niche Implants for an Animal Model Using 3D-Printed Molds, *Pharmaceutics*, 2023, **15**(6), 1584.
9 X. Zhao, T. Liao, Y. Lu, Z. Jiang and Y. Men, Formation and Distribution of the Mesophase in Ultrasonic Micro-Injection-Molded Isotactic Polypropylene, *Macromolecules*, 2021, **54**(11), 5167–5177.
10 M. Wang, W. Ding, Y. Xie, L. Zhang and Y. Chen, Effect of Micro-Mold Cavity Dimension on Structure and Property of Polylactic Acid/Polycaprolactone Blend under Microinjection Molding Conditions, *Polymers*, 2021, **13**(6), 887.
11 Y. Xie, H. Xiong, Z. Zheng, L. Zhang and Y. Chen, Facile and Scalable Fabrication of High-Performance Polylactide-Based Medical Microparts through Combining the Microinjection Molding Intense Shear Stress Field and Annealing Strategy, *Ind. Eng. Chem. Res.*, 2022, **61**(37), 13886–13897.
12 W. Yu, J. Gu, Z. Li, S. Ruan, B. Chen, C. Shen, L. J. Lee and X. Wang, Study on the Influence of Microinjection Molding Processing Parameters on Replication Quality of Polylactic Acid Microneedle Array Product, *Polymers*, 2023, **15**(5), 1199.

© 2026 The Author(s). Published by the Royal Society of Chemistry

Open Access Article. Published on 18 May 2026. Downloaded on 6/14/2026 9:49:24 PM. This article is licensed under a Creative Commons Attribution-NonCommercial 3.0 Unported Licence.

13 C. Yang, X.-H. Yin and G.-M. Cheng, Microinjection molding of microsystem components: new aspects in improving performance, *J. Micromech. Microeng.*, 2013, **23**(9), 093001.
14 B. Zhao, Y. Qiang, W. Wu and B. Jiang, Tuning Power Ultrasound for Enhanced Performance of Thermoplastic Micro-Injection Molding: Principles, Methods, and Performances, *Polymers*, 2021, **13**(17), 2877.
15 T. L. de Albuquerque, J. E. Marques Júnior, L. P. de Queiroz, A. D. S. Ricardo and M. V. P. Rocha, Polylactic acid production from biotechnological routes: A review, *Int. J. Biol. Macromol.*, 2021, **186**, 933–951.
16 L. Zhang, Y. Chen, J. Tan, S. Feng, Y. Xie and L. Li, Performance Enhancement of PLA-Based Blend Microneedle Arrays through Shish-Kebab Structuring Strategy in Microinjection Molding, *Polymers*, 2023, **15**(10), 2234.
17 C. I. Serra-Aguado, M. Llorens-Gámez, P. Vercet-Llopis, V. Martínez-Chicote, S. Deb and Á. Serrano-Aroca, Engineering Three-Dimensional-Printed Bioactive Polylactic Acid Alginate Composite Scaffolds with Antibacterial and In Vivo Osteoinductive Capacity, *ACS Appl. Mater. Interfaces*, 2022, **14**(48), 53593–53602.
18 L. Tan, J. Fu, F. Feng, X. Liu, Z. Cui, B. Li, Y. Han, Y. Zheng, K. W. K. Yeung, Z. Li, *et al*, Engineered probiotics biofilm enhances osseointegration via immunoregulation and anti-infection, *Sci. Adv.*, 2020, **6**(46), eaba5723.
19 H. Yang, B. Jia, Z. Zhang, X. Qu, G. Li, W. Lin, D. Zhu, K. Dai and Y. Zheng, Alloying design of biodegradable zinc as promising bone implants for load-bearing applications, *Nat. Commun.*, 2020, **11**(1), 401.
20 J. Liu, J. Huang, Y. Ying, L. Hu and Y. Hu, pH-sensitive and antibacterial films developed by incorporating anthocyanins extracted from purple potato or roselle into chitosan/polyvinyl alcohol/nano-ZnO matrix: Comparative study, *Int. J. Biol. Macromol.*, 2021, **178**, 104–112.
21 S. An, Q. Gong and Y. Huang, Promotive Effect of Zinc Ions on the Vitality, Migration, and Osteogenic Differentiation of Human Dental Pulp Cells, *Biol. Trace Elem. Res.*, 2017, **175**(1), 112–121.
22 Z. Wang, K. Nakagawa, K. Guan, Q. Song, S. Zhou, S. Tanaka, Y. Okamoto, A. Matsuoka, E. Kamio, G. Li, *et al*, Two-Dimensional Interlayer Space Induced Horizontal Transformation of Metal-Organic Framework Nanosheets for Highly Permeable Nanofiltration Membranes, *Small*, 2023, **19**(33), e2300672.
23 S. Jiang, J. Li, J. Fang and X. Wang, Fibrous-Structured Freestanding Electrodes for Oxygen Electrocatalysis, *Small (Weinheim an der Bergstrasse, Germany)*, 2021, **17**(9), e1903760.
24 R. Belgamwar, R. Verma, T. Das, S. Chakraborty, P. Sarawade and V. Polshettiwar, Defects Tune the Strong Metal-Support Interactions in Copper Supported on Defected Titanium Dioxide Catalysts for CO(2) Reduction, *J. Am. Chem. Soc.*, 2023, DOI: 10.1021/jacs.3c01336.
25 T. Zhang, S. Zeng, H. Jiang, Z. Li, D. Bai, Y. Li and J. Li, Leather Solid Waste/Poly(vinyl alcohol)/Polyaniline Aerogel with Mechanical Robustness, Flame Retardancy, and Enhanced Electromagnetic Interference Shielding, *ACS Appl. Mater. Interfaces*, 2021, **13**(9), 11332–11343.
26 X. Zhu, J. Wang, L. Cai, Y. Wu, M. Ji, H. Jiang and J. Chen, Dissection of the antibacterial mechanism of zinc oxide nanoparticles with manipulable nanoscale morphologies, *J. Hazard. Mater.*, 2022, **430**, 128436.
27 H. Yao, Y. Fan, E. S. T. Emre, N. Li, M. Ge, J. Wang and J. Wei, Alginate-modified ZnO anti-planktonic and anti-biofilm nanoparticles for infected wound healing, *Int. J. Biol. Macromol.*, 2024, 135739.
28 K. Gai, T. Zhang, Z. Xu, G. Li, Z. He, S. Meng, Y. Shi, Y. Zhang, Z. Zhu, X. Pei, *et al*, Biomimetic management of bone healing stages: MOFs induce tunable degradability and enhanced angiogenesis-osteogenesis coupling, *Chem. Eng. J.*, 2024, **493**, 152296.
29 H. Cai, T. Zhang, R. Dai, S. Song, R. Han, Y. Li and J. Chen, Effect of poly(ε-caprolactone) microfibers in poly(lactide-co-glycolide) based bone fixation plate on preventing dimensional shrinkage and promoting cell interactions, *Compos. Sci. Technol.*, 2021, **216**, 109051.
30 R. Han, L. Zheng, G. Li, G. Chen, S. Ma, S. Cai and Y. Li, Self-Poled Poly(vinylidene fluoride)/MXene Piezoelectric Energy Harvester with Boosted Power Generation Ability and the Roles of Crystalline Orientation and Polarized Interfaces, *ACS Appl. Mater. Interfaces*, 2021, **13**(39), 46738–46748.
31 P. Liu, X. Wang, X. Jia and J. Zhou, Carbon-Confined Two-Dimensional Sodiophilic Sites Boosted Dendrite-Free Sodium Metal Anodes, *ACS Appl. Mater. Interfaces*, 2022, **14**(31), 35873–35882.
32 A. J. Kennedy, A. Das, C. Williams, L. Slattery, S. Martin, M. Hull, C. Griggs and M. J. Bortner, Breaking Bad: Deagglomerating TiO(2) in 3D Printable Polymer Composites for Photocatalysis in Environmental Media, *ACS Appl. Mater. Interfaces*, 2026, **18**(7), 11430–11444.
33 R. Huang, X. Huang, Q. Zhang, J. Fan, Z. Zhang and J. Huang, Humidity-responsive pectin/AgNPs/ZnO composite films with high antimicrobial and UV-proof functions, *Int. J. Biol. Macromol.*, 2024, **279**(Pt 1), 135075.
34 R. L. Frost, Y. Xi and H. He, Synthesis, characterization of palygorskite supported zero-valent iron and its application for methylene blue adsorption, *J. Colloid Interface Sci.*, 2010, **341**(1), 153–161.
35 W. C. Liew, I. I. Muhamad, J. W. Chew and K. J. A. Karim, Synergistic effect of graphene oxide/zinc oxide nanocomposites on polylactic acid-based active packaging film: Properties, release kinetics and antimicrobial efficiency, *Int. J. Biol. Macromol.*, 2023, **253**(Pt 6), 127288.
36 Z.-T. Yang, J.-X. Yang, J.-H. Fan, Y.-H. Feng and Z.-X. Huang, Preparation of super-toughened Poly(L-lactide) composites under elongational flow: A strategy for balancing stiffness and ductility, *Compos. Sci. Technol.*, 2021, **208**, 108758.
37 Q. Yang, J. Yang, X. Liu, Y. Zhang, Y. Li, D. Ao, P. Zhong and K. Yong, Crosstalk Between the Mitochondrial Dynamics and Oxidative Stress in Zinc-induced Cytotoxicity, *Biol. Trace Elem. Res.*, 2023, **201**(9), 4419–4428.
38 Y. Tian, Y. Xu, J. Pinc, J. Fojt, V. Hybášek, J. Kubásek, Š. Msallamová, Y. Xiang, M. Guo, J. Čapek, *et al*,

Open Access Article. Published on 18 May 2026. Downloaded on 6/14/2026 9:49:24 PM.
This article is licensed under a Creative Commons Attribution-NonCommercial 3.0 Unported Licence.

Biodegradable Zn-0.8Mg-0.2Sr alloy as an internal fixation material exhibits controlled degradation with enhanced osteogenesis, *RSC Adv.*, 2025, **15**(37), 30071–30088.

39 X. Yuan, W. Zhu, Z. Yang, F. Chen and X. Han, Three-Dimensional Printing of Poly-L-Lactic Acid Composite Scaffolds with Enhanced Bioactivity and Controllable Zn Ion Release Capability by Coupling with Carbon-ZnO, *Bioengineering*, 2023, **10**(3), 307.

40 Y. Qin, Z. Jing, D. Zou, Y. Wang, H. Yang, K. Chen, W. Li, P. Wen and Y. Zheng, A metamaterial scaffold beyond modulus limits: enhanced osteogenesis and angiogenesis of critical bone defects, *Nat. Commun.*, 2025, **16**(1), 2180.

41 J. Y. Youn, W. H. Dunham, S. J. Hong, J. D. R. Knight, M. Bashkurov, G. I. Chen, H. Bagci, B. Rathod, G. MacLeod, S. W. M. Eng, *et al*, High-Density Proximity Mapping Reveals the Subcellular Organization of mRNA-Associated Granules and Bodies, *Mol. Cell*, 2018, **69**(3), 517–532.

42 D. Xing, W. Zuo, J. Chen, B. Ma, X. Cheng, X. Zhou and Y. Qian, Spatial Delivery of Triple Functional Nanoparticles via an Extracellular Matrix-Mimicking Coaxial Scaffold Synergistically Enhancing Bone Regeneration, *ACS Appl. Mater. Interfaces*, 2022, **14**(33), 37380–37395.

43 Y. Liu, D. Luo and T. Wang, Hierarchical Structures of Bone and Bioinspired Bone Tissue Engineering, *Small (Weinheim an der Bergstrasse, Germany)*, 2016, **12**(34), 4611–4632.

© 2026 The Author(s). Published by the Royal Society of Chemistry